International Journal of Greenhouse Gas Control 30 (2014) 9–18

Contents lists available at ScienceDirect

International Journal of Greenhouse Gas Control

journal homepage: www.elsevier.com/locate/ijggc

Modelling the non-equilibrium two-phase flow during depressurisation of CO_2 pipelines

S. Brown [a,*], S. Martynov [a], H. Mahgerefteh [a], S. Chen [b], Y. Zhang [b]

[a] Department of Chemical Engineering, University College London, London WC1E 7JE, United Kingdom
[b] Dalian University of Technology, Dalian, People's Republic of China

ARTICLE INFO

Article history:
Received 17 May 2014
Received in revised form 6 August 2014
Accepted 15 August 2014
Available online 7 September 2014

Keywords:
Multi-phase flow
CO_2 pipeline safety
Mathematical modelling

ABSTRACT

The development, testing and validation of a two-fluid transient flow model for simulating outflow following the failure of high pressure CO_2 pipelines is presented. Thermal and mechanical non-equilibrium effects during depressurisation are accounted for by utilising simple constitutive relations describing inter-phase mass, heat and momentum transfer in terms of relaxation to equilibrium. Pipe wall/fluid heat exchange on the other hand is modelled by coupling the fluid model with a finite difference transient heat conduction model. The two-fluid transient flow model's performance is tested by comparison of the predicted transient pressure and temperature profiles along the pipeline against those based on the simplified homogeneous equilibrium model (HEM) as well as real data captured during the full bore rupture of a 260 m long, 233 mm internal diameter pipeline containing CO_2 at 36 bara and 273 °C. The two-fluid model is found to produce a reasonably good degree of agreement with the experimental data throughout the depressurisation process. The HEM based flow model on the other hand performs well only near the rupture plane and during the early stages of the depressurisation process.

1. Introduction

The internationally agreed objective of limiting the increase in global average temperatures to less than 2 °C above pre-industrial levels requires a 50–80% reduction in CO_2 emissions by 2050 (Edenhofer et al., 2011). Alongside renewable energy sources CO_2 capture and storage (CCS) is widely considered as a key technology for meeting this target, potentially reducing the cost of inaction by some $2 trillion over the next 40 years (IEA, 2012).

It is estimated (IEA, 2010; Element Energy, 2010) that transporting the predicted 2.3–9.2 Gt of captured CO_2 to its point of storage will require the use of a global network of between 95,000 and 550,000 km of pipeline by 2050.

For the transportation of such large amounts of CO_2 to be economical the majority of CCS pipelines will need to be operated in the dense or supercritical-phase rather than in the vapour-phase (Roussanaly et al., 2013; Knoope et al., 2013). In Europe this will likely mean pipelines at line pressures above 100 bar passing through or near populated areas. Given that CO_2 is increasingly toxic at concentrations higher than 7% (v/v) (Kruse and Tekiela, 1996), the safety of CO_2 pipelines is of great importance and indeed pivotal to the public acceptability of CCS as a viable means for tackling the impact of global warming.

Central to assessing the safety of such pipelines is the accurate prediction of the decompression and the discharge rate of the escaping inventory in the event of accidental pipeline rupture. Such data forms the basis for determining the minimum safe distances to populated areas, emergency response planning and the optimum spacing of emergency shutdown valves.

The accurate modelling of the decompression process during pipeline rupture requires accounting for a number of complex and interacting phenomena. These include the tracking of sonic decompression waves propagating from the rupture plane towards the intact end of the pipeline, fluid/wall friction and heat transfer and well as real fluid behaviour. In the case of a volatile fluid such as dense-phase or supercritical CO_2, by far the biggest challenge is the correct modelling of the ensuing complex flow dynamics associated with the transition from single to two-phase flow.

In attempting to model the two-phase flow behaviour, the majority of pipeline depressurisation models reported in the literature have utilised the simplistic homogeneous equilibrium mixture (HEM) model (see for example Terenzi, 2005; Mahgerefteh et al., 2012; Popescu, 2009) where the constituent fluid phases are assumed to remain in thermal and mechanical equilibrium

* Corresponding author.
E-mail address: solomon.brown@ucl.ac.uk (S. Brown).

http://dx.doi.org/10.1016/j.ijggc.2014.08.013

Nomenclature

Roman symbols

$\dot{m}$	numerical mass flux
a	speed of sound
c_p	specific heat capacity
C_f	inter-phase friction coefficient
D_h	internal diameter of the pipe
E	fluid total energy
e	internal energy
f	Fanning friction factor
F^D	inter-phase drag force
F^{nv}	non-viscous forces
F^v	viscous friction forces
g	acceleration due to gravity vector
H	fluid specific total enthalpy
h	specific enthalpy
k	thermal conductivity
M	fluid Mach number
P	fluid pressure
P^{int}	interfacial pressure
Pr	Prandtl's number
q^i	heat exchange with the interface
q^w	heat exchange with the wall
R	gas constant
r	radial co-ordinate
Re	Reynold's number
T	temperature
t	time co-ordinate
u	fluid velocity
u^{int}	interfacial velocity
v	specific volume
x	axial co-ordinate

Greek symbols

α	volume fraction
η	heat transfer coefficient
Γ	mass transfer flux
ω	acentric factor
ρ	density
σ	numerical flux parameter
τ	thermal relaxation time

Subscripts

c	critical properties
ig	ideal gas properties
l	liquid phase
sat	saturated properties
v	vapour phase
w	wall properties

throughout the decompression process. Consequently important phenomena such as phase slip and non-equilibrium liquid/vapour transition are ignored.

During the course of our recently completed CO2PipeHaz FP7 project (CO2PipeHaz, 2012), for the first time we verified flow stratification based on the direct visual observation of the fluid flow patterns through a reinforced glass section of a ruptured 36 m long, 40 mm internal diameter (i.d.) pipeline containing dense phase CO_2 (at initial conditions of 70 bar, 20 °C). In the case of full bore rupture, the initial dispersed flow was observed to gradually transition to stratified flow as the pipeline depressurised. In the case of pipeline punctures however, the switch between the two flow regimes was found to be far more rapid.

Munkejord et al. (2010) accounted for phase slip by utilising the *drift flux* model. Through the application of their model to the decompression of CO_2/methane mixtures, the authors showed that phase slip had a significant impact on the pipeline decompression. In a recent publication, we (Brown et al., 2013) presented a *Homogeneous Relaxation Model* that accounted for the delay in vaporisation during the decompression of dense-phase CO_2. The application of the model to hypothetical pipeline rupture scenarios revealed that whilst the predicted depressurisation rates were similar to those obtained using the HEM model, the simulated discharge rates based on HRM were consistently up to 20% larger.

The compressible two-fluid model (see for the general formulation Stewart and Wendroff, 1984; Ishii and Hibiki, 2006) which has been widely used in the petroleum and nuclear industries (Bestion, 1990; Bendiksen et al., 1991) is in principle capable of simulating the inter-phase dynamics and flow regimes of interest. Here, the dynamics of each phase are described independently; however, in order to account for the interactions between the phases, empirical models are required for the heat, mass and momentum transfer effects. In the case of CO_2 the limited work reported on this topic (for interphase friction see Cheng et al., 2008) is restricted to steady-state two-phase CO_2 flows in small diameter tubes ($\leq$8 mm i.d.). It is uncertain whether these empirically driven correlations are applicable to transient releases from large diameter pipelines (Thome and Ribatski, 2005) of interest in CCS.

In this work the compressible two-fluid model is applied to simulate the decompression of CO_2 following pipeline failure. In the absence of dedicated empirical correlations for CO_2 relatively simple constitutive relations available in the literature are employed to account for inter-phase heat, mass and momentum exchanges. The sensitivity of the two-fluid model's predictions to these effects is investigated based on parametric studies involving variation of the relaxation time scale controlling the rate of the inter-phase heat and mass transfer. The predictions obtained are next compared against the measured decompression test data recorded for a CO_2 pipeline rupture test conducted as part of the FP7 project CO2PipeHaz (2012).

The work presented proceeds as follows. Section 2 presents the fluid dynamics model, the inter-phase relations, the friction and heat transfer model followed by the fluid properties package employed for predicting the required thermodynamic data. Section 3 presents the numerical method employed for the problem solution. Section 4 describes the pipeline rupture experimental set-up used for model validation. The results and discussion, encompassing the sensitivity analysis and comparison of the theoretical predictions against real data, is presented in Section 5. Section 6 presents the conclusions drawn.

2. Model formulation

2.1. Fluid dynamics

The rigorous description of transient flow during the decompression of compressible two-phase flow requires equations accounting for the behaviour of each constituent phase (see for example Ishii and Hibiki, 2006). Accordingly, in this work the single pressure two-fluid model (see e.g. Stewart and Wendroff, 1984) is applied to the two-phase flow of CO_2. This model may be written in the general form (see e.g. Paillere et al., 2003):

$$\frac{\partial \mathbf{U}}{\partial t} + \frac{\partial \mathbf{F}(\mathbf{U})}{\partial x} = \mathbf{C}^{nv} + \mathbf{C}^{v} + \mathbf{S}, \quad (1)$$

where

$$\mathbf{U} = \begin{pmatrix} \alpha_v\rho_v \\ \alpha_l\rho_l \\ \alpha_v\rho_v u_v \\ \alpha_l\rho_l u_l \\ \alpha_v\rho_v E_v \\ \alpha_l\rho_l E_l \end{pmatrix}, \ \mathbf{F}(\mathbf{U}) = \begin{pmatrix} \alpha_v\rho_v u_v \\ \alpha_l\rho_l u_l \\ \alpha_v\rho_v u_v^2 + \alpha_v P \\ \alpha_l\rho_l u_l^2 + \alpha_l P \\ \alpha_v\rho_v u_v H_v \\ \alpha_l\rho_l u_l H_l \end{pmatrix}, \tag{2}$$

u_k, ρ_k, E_k and H_k are respectively the velocity, density, total energy and specific total enthalpy for each phase k. P is the system pressure, while α_k are the volume fractions for which the following relation holds:

$$\alpha_v + \alpha_l = 1, \tag{3}$$

$\mathbf{C}^{nv}$ and $\mathbf{C}^{v}$ are the vectors of non-viscous differential terms and viscous non-differential terms respectively. These in turn are given by:

$$\mathbf{C}^{nv} = \begin{pmatrix} 0 \\ 0 \\ P\dfrac{\partial\alpha_v}{\partial x} + F_v^{nv} \\ P\dfrac{\partial\alpha_l}{\partial x} + F_l^{nv} \\ -P\dfrac{\partial\alpha_v}{\partial t} + u^{\text{int}}F_v^{nv} \\ -P\dfrac{\partial\alpha_l}{\partial t} + u^{\text{int}}F_v^{nv} \end{pmatrix}, \ \mathbf{C}^{v} = \begin{pmatrix} 0 \\ 0 \\ F_v^v \\ F_l^v \\ 0 \\ 0 \end{pmatrix}, \tag{4}$$

where u^{int}, F_k^{nv} and F_k^v are respectively the interfacial velocity, inter-phase forces containing derivative terms and viscous friction terms.

Finally $\mathbf{S}$ is the vector of non-differential source terms (such as gravity and phase change) given by:

$$\mathbf{S} = \begin{pmatrix} \Gamma_v \\ \Gamma_l \\ u^{\text{int}}\Gamma_v + F_v^D + \alpha_v\rho_v g_x \\ u^{\text{int}}\Gamma_l + F_l^D + \alpha_l\rho_l g_x \\ u^{\text{int}}F_v^D + H_l\Gamma_v + q_v^i + \dfrac{4q_v^w}{D_h} + \alpha_v\rho_v u_v g_x \\ u^{\text{int}}F_l^D + H_v\Gamma_l + q_l^i + \dfrac{4q_l^w}{D_h} + \alpha_l\rho_l u_l g_x \end{pmatrix}, \tag{5}$$

where Γ_k, F_k^D, H_k, q_k^i and q_k^w are respectively the mass transfer flux, the inter-phase drag force, specific total enthalpy and heat exchanged with the interface (i) and the wall (w) for phase k. D_h is the internal diameter of the pipe and g_x is the projection of the gravity vector onto the x-coordinate axis.

2.2. Constitutive relations

It is well known (Stuhmiller, 1977) that the two-fluid model is non-hyperbolic in the case $F_k^{nv} = 0$. Whence we follow the commonly used approach of applying the interfacial pressure correction force (Stuhmiller, 1977):

$$F_k^{nv} = (P^{\text{int}} - P)\frac{\partial\alpha_k}{\partial x}, \tag{6}$$

where

$$P^{\text{int}} = P - \sigma\frac{\alpha_v\rho_v\alpha_l\rho_l}{\alpha_v\rho_l + \alpha_v\rho_l}(u_v - u_l)^2, \tag{7}$$

values of $\sigma \geq 1$ enforce hyperbolicity. For the purposes of this work $\sigma = 2$ is used.

u^{int} is defined by the weighted average of the vapour and liquid velocities:

$$u^{\text{int}} = \alpha_v u_v + (1 - \alpha_v)u_l. \tag{8}$$

Following Cortes (2002), the inter-phase drag terms F_k^D are defined by:

$$F_v^D = -F_l^D = C_f\alpha_v^m\alpha_l^n(\kappa_l\rho_l + \kappa_v\rho_v)|v_v - v_l|(v_v - v_l). \tag{9}$$

Where C_f, m, n, κ_l and κ_v are the friction coefficient and flow regime dependent coefficients respectively. m and n are both unity, while $\kappa_l = 0.752$ and $\kappa_v = 0.01063$. The viscous friction terms are given by:

$$F_v^v = -\frac{2f\alpha_v\rho_v\,|v_v|\,v_v}{D_h} \tag{10}$$

and

$$F_l^v = -\frac{2f\alpha_l\rho_l\,|v_l|\,v_l}{D_h}, \tag{11}$$

where f is the Fanning friction factor, which is assumed to take the constant value of 0.017 (Garcia-Cascales et al., 2007). The q_k^i are taken to be (Garcia-Cascales et al., 2007):

$$q_v^i = \frac{C_\tau}{\tau}\alpha_v\alpha_l(h_{\text{sat},v} - h_v) \tag{12}$$

$$q_l^i = \frac{C_\tau}{\tau}\alpha_v\alpha_l(h_{\text{sat},l} - h_l) \tag{13}$$

where C_τ and τ are problem specific constants and the subscript sat indicates saturated properties. We use $C_\tau = 1$ throughout.

The above q_k^i are used to define the mass transfer fluxes:

$$\Gamma_v = -\Gamma_l = -\frac{(q_v^i + q_l^i)}{h_{\text{sat},v} - h_{\text{sat},l}}. \tag{14}$$

2.3. Heat conduction in pipe wall

In order to calculate the heat flux between the pipe wall and the fluid as a function of time the temperature of the wall must be calculated. To accomplish this the transient heat conduction equation for a two-dimensional cross section of the pipe wall (in cylindrical coordinates) is solved:

$$\frac{\partial T}{\partial t} = \frac{k_w}{\rho_w c_{p,w}}\left(\frac{1}{r}\frac{\partial}{\partial r}\left(r\frac{\partial T}{\partial r}\right) + \frac{\partial^2 T}{\partial x^2}\right), \tag{15}$$

where k_w, ρ_w and $c_{p,w}$ are respectively the pipe wall thermal conductivity, density and heat capacity and are assumed to take the constant values 53.65 $\text{W m}^{-1}\text{K}^{-1}$, 7850 kg m^{-3} and 460 $\text{J kg}^{-1}\text{K}^{-1}$, which are representative of carbon steel (Perry and Green, 1997). r, is the radial coordinate. Eq. (15) is solved numerically using a standard explicit, central difference method (Pletcher et al., 1997).

For simplicity, the pipe wall is assumed to be perfectly insulated so that the heat exchange with the surroundings may be ignored. Given the highly turbulent flow during depressurisation, we assume that only forced convective heat transfer occurs between both the flowing liquid and vapour phases and the inner pipe wall. Accordingly, the corresponding heat transfer coefficient, η is calculated using the Dittus-Boelter (1930) correlation:

$$\eta_k = 0.023Re_k^{0.8}Pr_k^{0.4}\frac{k_k}{(\alpha_k D_h)}, \tag{16}$$

where k_k, Re_k and Pr_k are the thermal conductivity, Reynold's number and Prandtl's number for each phase k respectively.

The q_k^w are then calculated from:

$$q_k^w = \eta_k\alpha_k(T_w - T_k) \tag{17}$$

where T_k and T_w are respectively the temperature for phase k and the temperature of the wall at the interior boundary. For the boundary along the pipe's thickness at the release point the same heat flux boundary condition as that present in Eq. (17) is applied with the further assumption that the fluid state is that of the exiting fluid.

2.4. Fluid physical properties

For the purpose of this study we consider pure CO_2, for which a growing number of Equations of State (EoS) have been proposed ranging in complexity from the reference Span and Wagner (1996) to those based on Statistical Associating Fluid Theory (Diamantonis and Economou, 2011). However, despite the accuracy of these EoS the computational effort required to couple them with the two-phase flow model developed in this work is prohibitive. To deal with this problem, as a starting point, we employ the far simpler Peng–Robinson (PR) EoS (Peng and Robinson, 1976):

$$P = \frac{RT}{v-b} - \frac{d\delta}{v^2+2bv-b^2}, \tag{18}$$

where v and R are the specific volume and the gas constant respectively. d, b and δ are respectively given by:

$$d = 0.45724\frac{(RT_c)^2}{P_c} \tag{19}$$

$$b = 0.07780\frac{RT_c}{P_c} \tag{20}$$

$$\delta = \left[1 + (0.37464 + 1.54226\omega - 0.26992\omega^2)\left(1 - \sqrt{\frac{T}{T_c}}\right)\right]^2. \tag{21}$$

Where T_c and ω are respectively the critical temperature and the acentric factor; along with P_c these are given by:

$$P_c = 72.44016 \quad \text{bara}, \quad T_c = 304.35 \quad \text{K} \quad \text{and} \quad \omega = 0.2236$$

From Eq. (18), the internal energy may be calculated using the identity (Poling et al., 2001):

$$e - e_{ig} = \int_{-\infty}^{v}\left[T\left(\frac{\partial P}{\partial T}\right)_v - P\right]dv \tag{22}$$

where the subscript, ig refers to ideal gas.

3. Numerical solution method

In this section the numerical method employed for the efficient solution of the system of Eq. (1) is presented. First the equations are integrated over a control volume, i, to yield the semi-discrete formulation as follows:

$$\frac{d\mathbf{U}_i}{dt} = -\frac{1}{\Delta x}(\mathbf{F}_{i+1/2} - \mathbf{F}_{i-1/2}) + \mathbf{C}_i^{nv} + \mathbf{C}_i^{v} + \mathbf{S}_i \tag{23}$$

The remaining problems of the specification of the inter-cell flux ($\mathbf{F}_(i+(1/2))$, the discretisation of the source terms and the temporal discretisation will be considered independently. Additionally, to increase the accuracy of the method while maintaining efficiency, an adaptive mesh refinement (AMR) methodology is applied.

3.1. Spatial discretisation

Numerous techniques have been presented for approximating the inter-cell fluxes ($\mathbf{F}_{i+(1/2)}$) based on approximate Riemann solvers (see for example Munkejord, 2007; Yeom and Chang, 2013) and kinetic schemes (see for example Coquel et al., 1997). In this study, we use the AUSM+ scheme (Liou, 2006), first adapted to the two-fluid model by Paillere et al. (2003) and further developed by Niu et al. (2008). Briefly, the AUSM+ scheme (Liou, 2006) proceeds by separating the phasic flux, $\mathbf{F}_k$ into convective and pressure terms:

$$\mathbf{F}_k = \dot{m}_k\begin{pmatrix}1\\u_k\\H_k\end{pmatrix} + \begin{pmatrix}0\\\alpha_k P\\0\end{pmatrix} = \dot{m}_k\boldsymbol{\Psi}_k + \mathbf{P}_k. \tag{24}$$

The inter-cell flux is then defined as:

$$\mathbf{F}_{i+(1/2)} = \dot{m}_k^{\star}\boldsymbol{\Psi}_k^{\star} + \mathbf{P}_k^{\star}, \tag{25}$$

where

$$\dot{m}_k^{\star}\boldsymbol{\Psi}_k^{\star} = \dot{m}_k^{\star}\frac{1}{2}(\boldsymbol{\Psi}_{k,i} + \boldsymbol{\Psi}_{k,i+1}) + \frac{1}{2}|\dot{m}_k^{\star}|(\boldsymbol{\Psi}_{k,i} - \boldsymbol{\Psi}_{k,i+1}). \tag{26}$$

It remains then to define $\dot{m}_k^{\star}$ and $(\alpha_k P)^{\star}$. First the interface speed of sound a is defined as:

$$a_{k,i+(1/2)} = \sqrt{a_{k,i}a_{k,i+1}}, \tag{27}$$

and the left and right phasic Mach numbers, M_k:

$$M_{k,i} = \frac{u_{k,i}}{a_{k,i+(1/2)}} M_{k,i+1} = \frac{u_{k,i+1}}{a_{k,i+(1/2)}}. \tag{28}$$

Then:

$$(\alpha_k P)_{i+(1/2)} = \mathcal{P}^{+}(M_i)(\alpha_k P)_i + \mathcal{P}^{-}(M_{i+1})(\alpha_k P)_{i+1} \tag{29}$$

$$M_{i+(1/2)} = \mathcal{M}^{+}(M_i) + \mathcal{M}^{-}(M_{i+1}) \tag{30}$$

where $\mathcal{M}^{+}$ and $\mathcal{M}^{-}$ are the polynomials introduced by Liou (1996):

$$\mathcal{M}_1^{\pm} = \frac{1}{2}\left(M \pm \left|M\right|\right) \tag{31}$$

$$\mathcal{M}_2^{\pm} = \pm\frac{1}{4}(M \pm 1)^2 \tag{32}$$

$$\mathcal{M}_4^{\pm} = \begin{cases}\mathcal{M}_1^{\pm}/M & \text{when } |M| \geq 1\\ \pm\mathcal{M}_2^{\pm}(1 \mp 16B\mathcal{M}_2^{\mp}) & \text{else}\end{cases} \tag{33}$$

$$\mathcal{P}^{\pm} = \begin{cases}\mathcal{M}_1^{\pm}/M & \text{when } |M| \geq 1\\ \pm\mathcal{M}_2^{\pm}(2 \mp M - 16AM\mathcal{M}_2^{\mp}) & \text{else}\end{cases} \tag{34}$$

with $A = 3/16$ and $B = 1/8$.

Finally, we define:

$$\dot{m}_k^{\star} = \dot{a}_{k,i+(1/2)}\left[\frac{\rho_{k,i}\alpha_{k,i}}{2}\left(M_{k,i+(1/2)} + \left|M_{k,i+(1/2)}\right|\right) + \frac{\rho_{k,i+1}\alpha_{k,i+1}}{2}\left(M_{k,i+(1/2)} - \left|M_{k,i+(1/2)}\right|\right)\right] \tag{35}$$

While the above scheme has proven to be remarkably robust, at low Mach numbers the approximation approaches a central difference and can suffer from odd-even decoupling (Liou, 1996). In order to suppress this, velocity based dissipation (Niu et al., 2008; Paillere et al., 2003) was introduced, following Liou et al. (2008) an additional term is added to Eq. (30) such that:

$$M_{k,i+(1/2)} = M_{k,i+(1/2)} - K_p\max(1 - \bar{M}^2, 0)\frac{P_{i+1} - P_i}{\bar{\rho}\bar{a}^2}, \tag{36}$$

where $\bar{M}$, $\bar{\rho}$ and $\bar{a}$ represent the arithmetic-averages of the i and $i+1$ values of the respective variables, and K_p is a constant set to unity in this study. The discretisation of the source terms follows Paillere et al. (2003), where the non-differential source terms and spatial derivatives in Eq. (4) are approximated using central differences. The time derivatives at time level n are taken to be:

$$\left(P\frac{\partial\alpha}{\partial t}\right)^n = P_i^n\frac{\alpha_i^n - \alpha_i^{n-1}}{\Delta t^{n-1}}, \tag{37}$$

where Δt^{n-1} is the previous time step.

3.2. Temporal discretisation

In this work the semi-discrete formulation is integrated in time using an rth stage second order low storage strong stability preserving Runge–Kutta presented by Ketcheson (2008) denoting the terms on the left hand side of Eq. (23) by the operator $\mathcal{L}$):

$$\mathbf{U}^0 = \mathbf{U}^t \tag{38}$$

$$\mathbf{U}^i = \sum_{j=0}^{i-1} (\beta_{i,j}\mathbf{U}^j + \Delta t \gamma_{i,j}\mathcal{L}(t_n + c_{k-1}\Delta t, \mathbf{U}^j)) \tag{39}$$

$$\mathbf{U}^{t+\Delta t} = \mathbf{U}^s, \tag{40}$$

where $i = 1 \ldots s$ and $s = 4$ is used throughout this work. β, γ and c are constants, of which the non-zero values are given by Ketcheson (2008)

$$\beta_{i,i-1} = \begin{cases} \dfrac{1}{s-1} & 1 \le i \le s-1, \\ \dfrac{1}{s} & i = s, \end{cases} \tag{41}$$

$$\gamma_{i,i-1} = \begin{cases} 1 & 1 \le i \le s-1, \\ \dfrac{s-1}{s} & i = s, \end{cases} \tag{42}$$

$$\gamma_{s,0} = \frac{1}{s} \tag{43}$$

$$c_i = \frac{i-1}{s-1} \tag{44}$$

Finally, the time step Δt is calculated using the following CFL-type condition (Paillere et al., 2003):

$$\Delta t = \lambda \max_{i \in \mathcal{I}} \left[\frac{\alpha_v \Delta x}{|u_{v,i}| + a_{v,i}} + \frac{\alpha_l \Delta x}{|u_{l,i}| + a_{l,i}} \right], \tag{45}$$

where λ is a C.F.L.-like number taken to be 0.3 throughout. This time step is also applied to the heat conduction in the pipe-wall.

3.3. Adaptive mesh refinement (AMR)

In order to further reduce the computational workload required for the resolution of the flow model, the numerical technique and equations presented above are implemented within an AMR code (Berger and Oliger, 1984; Rendleman et al., 2000). An essential part of this methodology is an accurate error estimator employed to define the region where mesh refinement is required. In this work the *a priori* error indicator suggested by Ziegler (2008) is applied to all conserved variables. Additionally, a small amount of artificial viscosity is added to the centrally discretised source terms to suppress oscillations at the interface between refinement levels.

4. Experimental set-up

The following describes the pipeline rupture experimental set-up and conditions for the CO_2 pipeline release experiments conducted as part of the FP7 funded CO2PipeHaz project (2012).

Fig. 1 shows a photograph of the fully instrumented 256 m long, 233 mm i.d. and 20 mm wall thickness test pipeline. Located in the Liaohe Oil Field in South West China, the pipeline is made of 16 Mn Carbon Steel with a maximum safe operating pressure of 200 bara. At one end, the pipeline incorporates a Full Bore Rupture (FBR) disc mechanism with provision to incorporate various size orifice flanges at a short distance (*ca.* 1 m) downstream from it. This provision provides a range of puncture diameters up to FBR. The other end of the pipe is connected to a feed line via an isolation valve. The temperature of the fluid within the pipeline may be adjusted to ±2 °C from ambient to a maximum of 50 °C using a 50 kW heating tape wound around its entire length. To minimise the heat exchange between the pipe and the surrounding air during the release experiments, the pipeline is insulated with *ca.* 50 mm thick glass wool and wrapped with 0.5 mm thick outer aluminium layer. The fluid pressure and temperature are measured using 12 low-temperature fast-response (13 mHz) pressure transducers (1–160 bar range, ±1% accuracy) and 18 K-type thermocouples (−70 to 100 °C range; ±1.5 °C accuracy; 1 mHz) strategically distributed along the pipe length. Table 1 presents the locations of the transducers along the pipeline.

Fig. 1. Photograph of an instrumented 256 m long, 233 mm i.d. pipeline for experimental studies of CO_2 releases.

5. Results and Discussion

In the following, the flow model developed in Section 2.1 is employed to simulate the transient decompression following the pipeline FBR test performed. The study is conducted to investigate the impact of the flow model's constitutive parameters on the simulated in-pipe transient pressure and temperatures during the pipeline decompression as compared to the recorded data. In particular, the effects of thermal relaxation time (τ), mechanical relaxation (C_f) and fluid/pipe wall heat exchange are investigated. For the sake of comparison, the corresponding predictions using the HEM model (Mahgerefteh et al., 2012) are also presented.

Prior to rupture, the pipeline is filled with *ca.* 5.6 tonnes of CO_2, containing 0.2% (v/v) of air, at saturation conditions 36 bara and 274 K with a corresponding vapour fraction $\alpha_v = 0.5$. The ambient pressure is 1 bara.

The simulations are performed using a spatial discretisation with two levels of refinement, the coarsest level containing 100 cells. The heat exchange between the pipe and the surroundings is considered negligible given that the pipe is thermally insulated. Unless otherwise stated the thermal relaxation time, τ and interphase friction coefficient, C_f are taken as $\tau = 5 \times 10^{-5}$ s and unity respectively.

Table 1
Pressure transducer and thermocouple positions relative to the high pressure end.

Location (m)	Pressure transducer	Thermocouples
249.6	P2	T3
245.6	P3	T4
241.7		T5
237.7	P4	T6
116.5	P8	

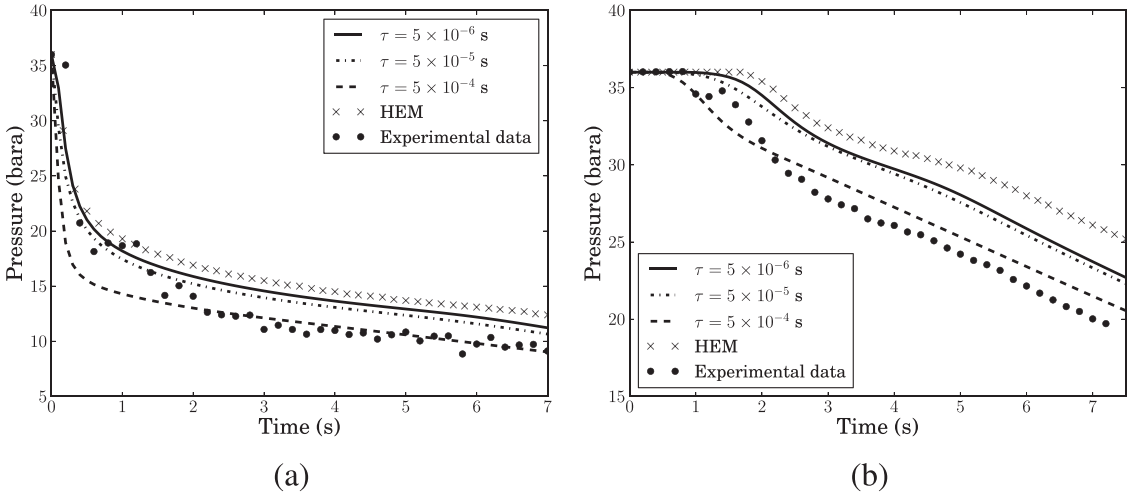

Fig. 2. Variation of fluid pressure at P2 (a) and P8 (b) with time following the initiation of decompression predicted using various thermal relaxation times (τ) and the experimental data.

5.1. *Influence of thermal relaxation time*

Fig. 2 (a) and (b) respectively show the predicted variation of pressure with time at transducers P2 (6.4 m from the rupture plane) and P8 (139.5 m from the rupture plane) following FBR for thermal relaxation times, τ, ranging from 5×10^{-6} to 5×10^{-4} s. Also shown in the same figure are the corresponding recorded experimental data and the HEM model (i.e. τ, $C_f \rightarrow 0$) predictions.

As may be observed from the data in Fig. 2(a) the experimental data show three distinct trends. In order of appearance these include:

1 a pressure plateau corresponding to the time taken for the decompression wave to reach the pressure transducer;
2 a marked rapid pressure drop corresponding to the arrival of the decompression wave followed by a second pressure plateau;
3 a relatively slow depressurisation rate commencing with the passage of the decompression wave from the transducer location.

From Fig. 2(a) (transducer P2) it can be seen that the simulations capture the initial rapid decline in the measured pressure during the first *ca.* 0.5 s following depressurisation. Lower pressure drops are observed as the relaxation time decreases, with the case $\tau = 5 \times 10^{-5}$ s showing the best agreement with the experimental data. Post *ca.* 0.5 s corresponding to the slower pressure decay region, the degree of agreement with the experimental data improves as the relaxation time increases, with HEM producing the worst predictions.

Very similar trends in the data may be observed in Fig. 2(b) as with Fig. 2(a), albeit at a slower depressurisation rate, given the longer distance of the pressure transducer position from the rupture plane. Also, in all cases, the pressure plateau prior to the arrival of the decompression wave is more clearly evident as compared to the data in Fig. 2(a).

Interestingly, in this case (Fig. 2(b)) the predictions of the arrival of the decompression wave are significantly affected by the thermal relaxation time; in particular as τ is increased the decompression begins earlier, i.e. 1 s for $\tau = 5 \times 10^{-4}$ compared to ca. 1.8 s for $\tau = 5 \times 10^{-6}$ s. Additionally, a slight deflection in the pressure is observed experimentally at ca. 4.5 s due to the reflection of the decompression wave from the closed end of the pipeline. The experimental data is in close agreement with the results using $\tau = 5 \times 10^{-4}$ s with regards the arrival of the decompression wave and also during the subsequent pressure drop.

The above observations highlight the necessity of accounting for the non-equilibrium effects from the commencement of decompression given their impact on the depressurisation trajectory.

Fig. 3(a) and (b) show the comparison of the experimental data with predictions of the liquid temperature at thermocouples T3 (6.4 m from the rupture plane) and T6 (18.3 m from the rupture plane) respectively. As may be observed, the measured temperature profiles show similar trends to the pressure data (see Fig. 2(a) and (b)). The initial rapid temperature drop is followed by a decline in the rate of cooling. Also, as in the pressure data, a short duration plateau (*ca.* 0.5 s) in the measured temperature at the beginning of the depressurisation may be observed. As expected, a higher degree of cooling may be observed in the case of thermocouple T3 given its closer proximity to the rupture plane.

At both thermocouple positions, the longest relaxation time of $\tau = 5 \times 10^{-4}$ s produces the worse agreement with the recorded temperatures. For all the remaining cases, relatively good agreement may be observed between theory and experiment with little discernable differences in model performance.

Fig. 4(a) and (b) show the comparison of the experimental data presented above with the predicted vapour-phase temperatures. The same general trends as for the liquid-phase are clear, but with a slightly greater degree of cooling. The exception to this is where $\tau = 5 \times 10^{-4}$ s, for which a far greater discrepancy with the measurements, of up to 15 K at T3 and 10 K at T6 is evident. These results and those presented in Fig. 3 are expected as the longer thermal relaxation times result in lower heat transfer between the liquid and vapour, hence producing a higher temperature difference between the phases.

It is important to note that there is likely to be a degree of lag in the experimental temperature measurements, and hence that the actual temperatures of the fluid during the early stages of decompression may be lower than recorded by the thermocouples. Clearly from Fig. 4(a) and (b) any lag in the thermocouple response would increase the degree of agreement with the predicted vapour temperatures.

To elucidate the phase behaviour during the depressurisation, Fig. 5 shows the thermodynamic trajectory of the CO_2 decompression at the collocated pressure transducer–thermocouple pair P2 and T3, relative to the CO_2 saturation line. Also shown are the trajectories of the liquid-phase obtained using the simulations presented

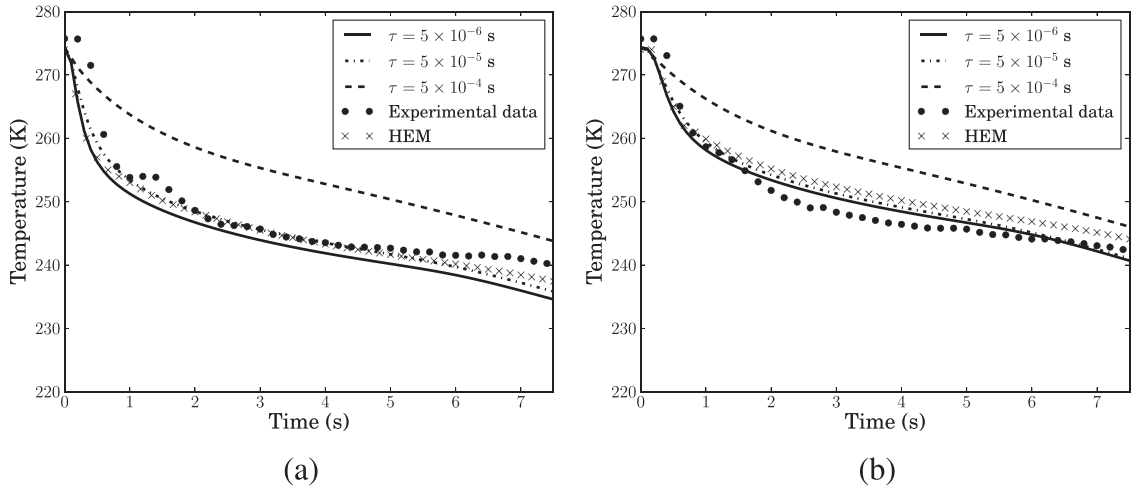

Fig. 3. Variation of liquid-phase temperature at T3 (a) and T6 (b) with time following the initiation of decompression predicted using various thermal relaxation times (τ) and the experimental data.

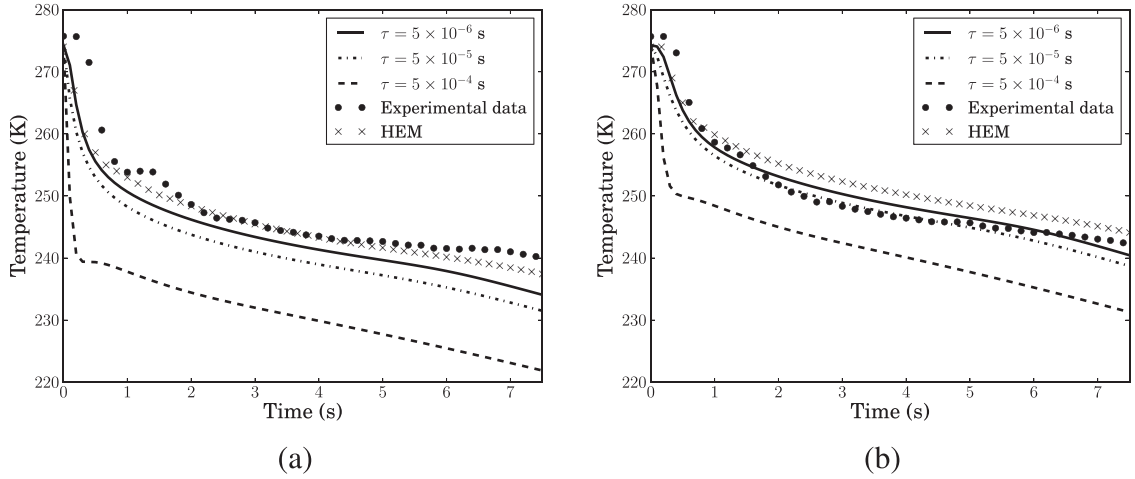

Fig. 4. Variation of vapour-phase temperature at T3 (a) and T6 (b) with time following the initiation of decompression predicted using various thermal relaxation times (τ) and the experimental data.

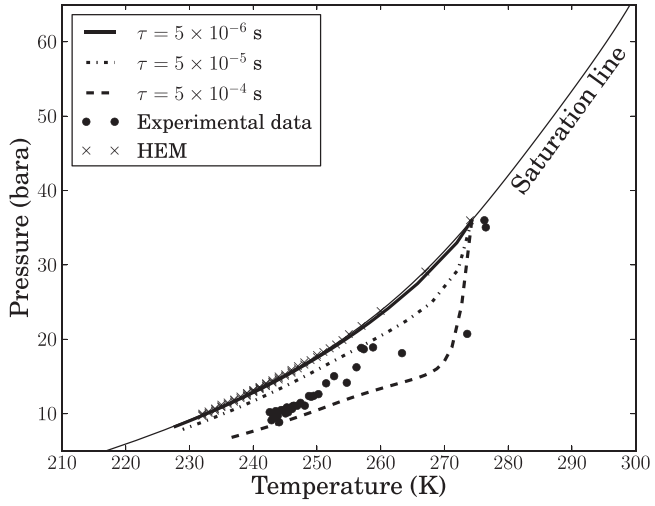

Fig. 5. Thermodynamic trajectories during decompression at P2–T3 relative to the saturation line of CO_2.

above. As can be seen the experimental data shows three distinct trends relative to the phase boundaries:

1 a pressure drop of ca. 20 bara from the initial state accompanied by a temperature drop of less than 4 K. This results in the fluid falling into the meta-stable region for the liquid content of the mixture;
2 a temperature drop from ca. 274 to 257 K, i.e. almost the saturation temperature, at constant pressure;
3 finally, the decompression continues parallel to the saturation line.

The predictions using $\tau = 5 \times 10^{-4}$ s produce a reasonable approximation of the first of these trends which, with reference to Fig. 2(a), occurs in under ca. 0.3 s. The results obtained with $\tau = 5 \times 10^{-5}$ s diverge visibly from the saturation line, while those using $\tau = 5 \times 10^{-6}$ s as well as the HEM model both remain on the saturation line throughout. This comparison shows that the HEM is incapable of producing reasonable predictions for this scenario, as the departure from thermodynamic equilibrium is too great for the flow to be approximated accurately.

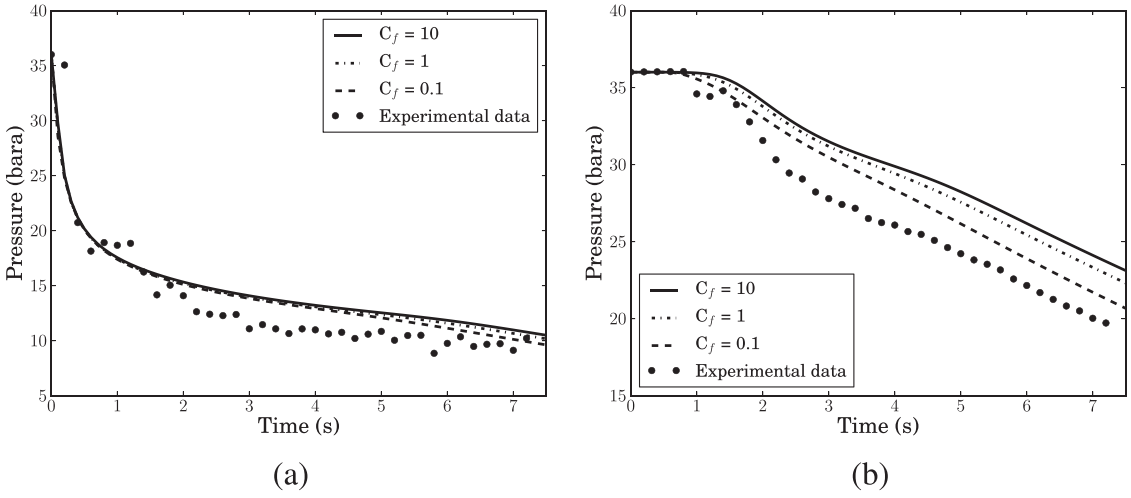

Fig. 6. Variation of fluid pressure at P2 (a) and P8 (b) with time following the initiation of decompression predicted using various interphase friction coefficients (C_f) and the experimental data.

5.2. Influence of inter-phase drag

Fig. 6(a) and (b) show the pressure predictions for inter-phase friction coefficients (C_f) ranging from C_f = 10 to 0.1 along with the experimental data for transducer positions P2 and P8 respectively. As may be observed in Fig. 6(a), reasonably good (*ca.* 2 bar max) agreement with the measured data may be observed in the first *ca.* 1 s following rupture. Beyond this point however, the simulations over predict the measured data by *ca.* 3 bara. Also at this transducer position and within the ranges tested, C_f has little impact on the simulations.

Similar trends in the data, albeit at a smaller rate of drop in pressure, may be observed in the case of the results presented in Fig. 6(b) with the exception of C_f having a marked impact on the predictions. Here the degree of agreement with the measured data reduces as C_f is increased.

5.3. Fluid/pipe wall heat transfer

In the pipeline rupture release experiments, although the pipe wall was insulated, and hence did not exchange heat with the surroundings, the initially warm steel pipe wall represented a significant source of heat. To simulate the impact of heat exchange between the flowing fluid and the pipe wall during the decompression, the flow model was coupled with the transient pipe wall heat conduction model described in Section 2.3. Prior to initiation of the release, the pipe wall is assumed to be in thermal equilibrium with the fluid. For the numerical solution of the heat conduction equation the pipe wall is discretised using an orthogonal mesh with the nodes at the internal wall collocated with those used for the fluid calculations.

Fig. 7(a) and (b) show the comparison of the liquid temperature predictions assuming adiabatic flow and those obtained accounting for pipe wall/fluid heat transfer model at T3 (6.4 m from rupture plane: Fig. 7(a)) and T5 (14.3 m from the rupture plane; Fig. 7(b)) against experimental data. As may be observed, in all cases, there is good accord between theory and experiment with no discernible difference in the performance between the two models as compared to the experimental data. Also, as expected, at any given time during the depressurisation process, the liquid temperature predicted by the non-adiabatic model is higher than that based on the adiabatic model.

Similar conclusions may be drawn based on the data in Fig. 8(a) and (b) showing the corresponding predictions for the vapour temperatures against the experimental data. It can be seen that accounting for fluid wall heat transfer has a slightly smaller impact

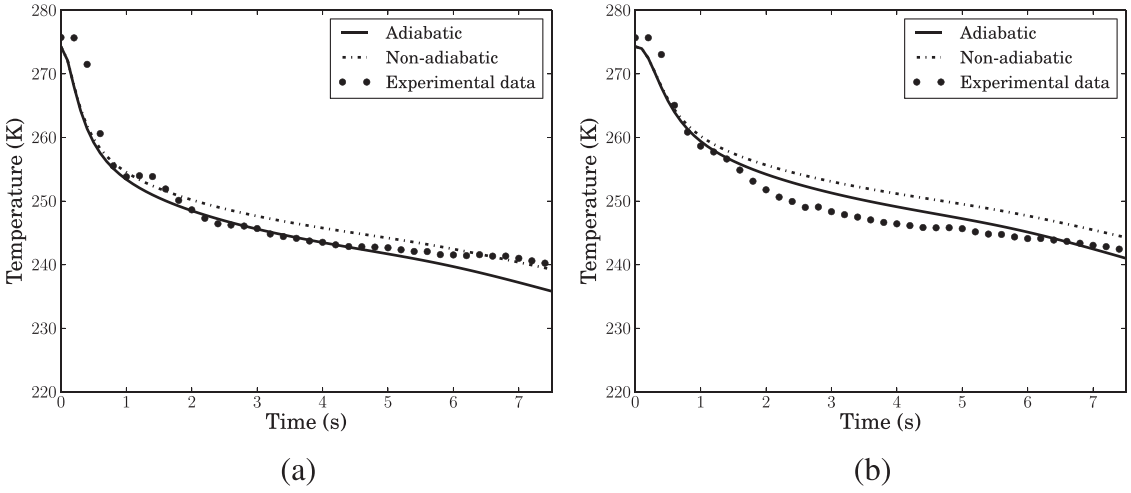

Fig. 7. Variation of liquid-phase temperature at T3 (a) and T6 (b) with time following the initiation of decompression predicted with adiabatic and non-adiabatic models and the experimental data.

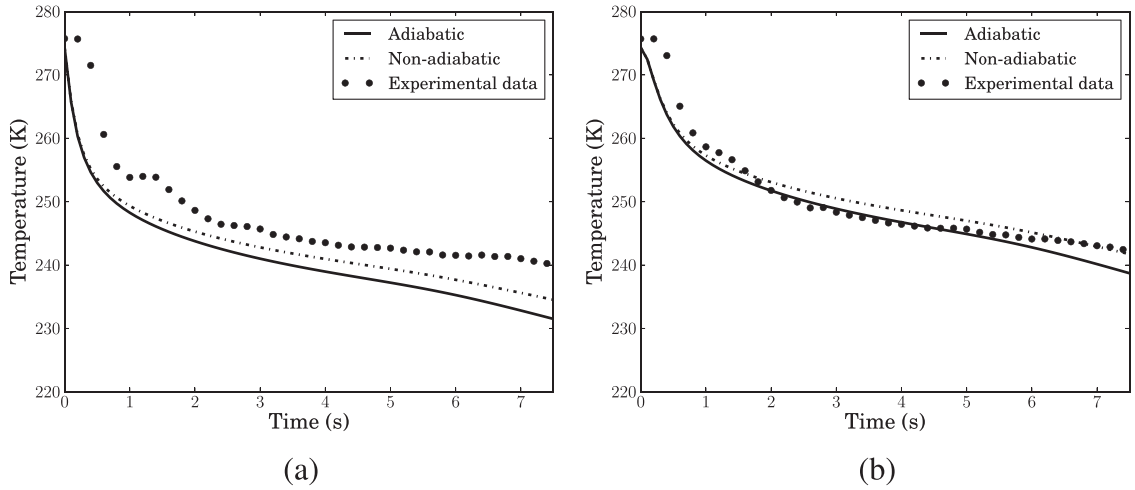

Fig. 8. Variation of vapour-phase temperature at T3 (a) and T6 (b) with time following the initiation of decompression predicted with adiabatic and non-adiabatic models and the experimental data.

on the predicted vapour temperatures as compared to the liquid-phase. This is due to the smaller heat transfer coefficient in the gaseous phase.

6. Conclusion

In this paper a non-equilibrium two-phase model describing fully compressible transient vapour-liquid flow was developed for simulating the depressurisation of high pressure CO_2 pipelines. The model accounted both for phase slip and delayed phase transitions, and incorporated a cubic equation of state for the accurate prediction of pertinent fluid thermodynamic properties. The performance of the model was investigated by comparison with pressure and temperature data measured in a large-scale CO_2 pipeline decompression test as well as those predicted using the simpler HEM.

Given the uncertainty about the applicability of existing non-equilibrium two-phase models for flashing CO_2 flows, the phase interaction terms including friction and heat and mass transfer were modelled using simple constitutive relations, assuming a constant thermal relaxation time and inter-phase drag coefficient. Similarly, the fluid/pipe wall heat transfer was assumed to be via forced convection. It was shown that the predictions obtained were in reasonably good agreement with the experimental data, but were strongly dependent on the thermal relaxation time, which characterises the rate of inter-phase heat and mass transfer. In particular, better agreement between predictions and the measured pressures was obtained with increasing thermal relaxation time during the later stages of the depressurisation. Interestingly however, at the location closest to the release end of the pipe, for the initial *ca.* 1 s of the decompression, the smallest relaxation time produced the best agreement. This transition had a more significant impact on the temperature predictions where, due to a sudden drop in the temperature, the predictions with the longer thermal relaxation time were found to be the least accurate.

The phase slip between the two phases was found to affect the predicted rate of decompression only at the locations furthest away from the release end of the pipe. This is likely due to the relatively low momentum of the flow in this region in comparison to that at the release point. Here, the results indicated that increasing the degree of slip produced faster decompression and a better agreement with the experimental data. However, it should be noted that the performance of inter-phase friction model cannot properly be assessed independently of the inter-phase heat and mass transfer predictions. The coupling of the model for the fluid flow with that for the heat conduction in the pipe wall had only a small impact on the results, though this was more pronounced close to the open end of the pipeline which is characterised by low temperatures and high fluid velocities. For longer duration releases, once the pressure gradients have been reduced, the thermal interaction between the fluid and pipe wall can be expected to have a more substantial effect on the decompression.

In summary, the predictions obtained from the two-fluid non-equilibrium model show better agreement with the experimental data in comparison with the commonly used HEM model. The latter was found to provide reasonable predictions only for the first 0.5 s of the decompression process and close to the release plane (for the case presented, within 30 m of the rupture plane). It should be noted that the performance of the HEM and the two-fluid models, in terms of degree of agreement with the measured data. is to a large extent dependent on the accuracy of the equation of state employed. For simplicity, in this study we used the PR EoS, which is not particularly suited to dense-phase CO_2. Furthermore, the simulations presented in this work were for Full Bore Rupture, where the two-phase flow is expected to be closer to homogeneous equilibrium behaviour as compared to pipeline puncture. Here the slower flow rate along with the more confined expansion through the puncture aperture will result in phase slip and delayed phase disengagement. Clearly, the ongoing development of the two-fluid presented here, and its application to puncture failure scenarios, provides a benchmark with which more simplified models used within the process safety industry may be assessed.

Acknowledgements

This work was supported by the UK Engineering and Physical Science Research Council (EPSRC reference EP/K000446/1) and the European Union 7th Framework Programme FP7-ENERGY-2012-1-2STAGE under grant agreement number 309102.

References

Bendiksen, K.H., Maines, D., Moe, R., Nuland, S., 1991. The dynamic two-fluid model OLGA: theory and application. Production 6 (6), 171–180.
Berger, M., Oliger, J., 1984. Adaptive mesh refinement for hyperbolic partial differential equations. J. Comput. Phys. 53 (3), 484–512.
Bestion, D., 1990. The physical closure laws in the CATHARE code. Nucl. Eng. Des. 124 (3), 229–245.
Brown, S., Martynov, S., Mahgerefteh, H., Proust, C., 2013. A homogeneous relaxation flow model for the full bore rupture of dense phase CO_2 pipelines. Int. J. Greenh. Gas Control 17, 349–356.

Cheng, L., Ribatski, G., Quiben, J.M., Thome, J.R., 2008. New prediction methods for CO_2 evaporation inside tubes: Part I. A two-phase flow pattern map and a flow pattern based phenomenological model for two-phase flow frictional pressure drops. Int. J. Heat Mass Transf. 51 (1–2), 111–124.

CO2PipeHaz, 2012. http://www.co2pipehaz.eu/index.php, accessed 05.07.12].

Coquel, F., Amine, K.E., Godlewski, E., Perthame, B., Rascle, P., 1997. A numerical method using upwind schemes for the resolution of two-phase flows. J. Comput. Phys. 136 (2), 272–288.

Cortes, J., 2002. On the construction of upwind schemes for non-equilibrium transient two-phase flows. Comput. Fluids 31 (2), 159–182.

Diamantonis, N.I., Economou, I.G., 2011. Evaluation of statistical associating fluid theory (SAFT) and perturbed chain-SAFT equations of state for the calculation of thermodynamic derivative properties of fluids related to carbon capture and sequestration. Energy Fuels 25 (7), 3334–3343.

Dittus, F., Boelter, L., 1930. Heat Transfer in Automobile Radiators of the Tubular Type. University of California Press, CA.

Edenhofer, O., Pichs-Madruga, R., Sokona, Y., Seyboth, K., Arvizu, D., Bruckner, T., Christensen, J., Devernay, J.-M., Faaij, A., Fischedick, M., Goldstein, B., Hansen, G., Huckerby, J., Jäger-Waldau, A., Kadner, S., Kammen, D., Krey, V., Kumar, A., Lewis, A., Lucon, O., Matschoss, P., Maurice, L., Mitchell, C., Moomaw, W., Moreira, J., Nadai, A., Nilsson, L., Nyboer, J., Rahman, A., Sathaye, J., Sawin, J., Schaeffer, R., Schei, T., Schlömer, S., Sims, R., Verbruggen, A., von Stechow, C., Urama, K., Wiser, R., Yamba, F., Zwickel, T., 2011. IPCC Special Report on Renewable Energy Sources and Climate Change Mitigation – Complete Report.

Element Energy, 2010. CO_2 Pipeline Infrastructure: An Analysis of Global Challenges and Opportunities. Tech. Rep., Final Report for IEA Greenhouse Gas Programme.

Garcia-Cascales, J.R., Mulas-Pérez, J., Paillère, H., 2007. Advances in the characterization of transient two-phase flow. AIAA J. 45 (10), 2579–2584.

IEA, 2010. Energy Technology Perspectives 2010: Scenarios and Strategies to 2050. Tech. Rep., OECD/IEA.

IEA, 2012. Energy Technology Perspectives 2012: Pathways to a Clean Energy System.

Ishii, M., Hibiki, T., 2006. Thermo-Fluid Dynamics of Two-Phase Flow. Smart Energy Systems. Springer, New York.

Ketcheson, D.I., 2008. Highly efficient strong stability preserving Runge–Kutta methods with low-storage implementations. SIAM J. Sci. Comput. 30 (4), 2113–2136.

Knoope, M., Ramírez, A., Faaij, A.P.C., 2013. A state-of-the-art review of techno-economic models predicting the costs of CO_2 pipeline transport. Int. J. Greenh. Gas Control 16, 241–270.

Kruse, H., Tekiela, M., 1996. Calculating the consequences of a CO_2-pipeline rupture. Energy Convers. Manage. 37 (95), 1013–1018.

Liou, M., 1996. A sequel to AUSM: AUSM+. J. Comput. Phys. 129 (2), 364–382.

Liou, M., 2006. A sequel to AUSM: Part II. AUSM+-up for all speeds. J. Comput. Phys. 214 (1), 137–170.

Liou, M., Chang, C., Nguyen, L., Theofanous, T.G., 2008. How to solve compressible multifluid equations: a simple, robust, and accurate method. AIAA J. 46 (9), 2345–2356.

Mahgerefteh, H., Brown, S., Denton, G., 2012. Modelling the impact of stream impurities on ductile fractures in CO_2 pipelines. Chem. Eng. Sci. 74, 200–210.

Munkejord, S., 2007. Comparison of Roe-type methods for solving the two-fluid model with and without pressure relaxation. Comput. Fluids 36 (6), 1061–1080.

Munkejord, S.T., Jakobsen, J.P., Austegard, A., Mølnvik, M.J., 2010. Thermo- and fluid-dynamical modeling of two-phase multicomponent carbon dioxide mixtures. Int. J. Greenh. Gas Control 4 (4), 589–596.

Niu, Y.-Y., Lin, Y.-C., Chang, C.-H., 2008. A further work on multi-phase two-fluid approach for compressible multi-phase flows. Int. J. Numer. Methods Fluids 58 (8), 879–896.

Paillere, H., Corre, C., Garcıa Cascales, J., 2003. On the extension of the AUSM+ scheme to compressible two-fluid models. Comput. Fluids 32 (6), 891–916.

Peng, D.-Y., Robinson, D.B., 1976. A new two-constant equation of state. Ind. Eng. Chem. Fundam. 15 (1), 59–64.

Perry, R.H., Green, D.W., 1997. Perry's Chemical Engineers' Handbook, 7th ed. McGraw-Hill, New York.

Pletcher, R., Tannehill, J., Anderson, D., 1997. Computational Fluid Mechanics and Heat Transfer. Series in Computational and Physical Processes in Mechanics and Thermal Sciences, 2nd ed. Taylor & Francis, Washington, DC.

Poling, B., Prausnitz, J., O'Connell, J., 2001. The Properties of Gases and Liquids. McGraw-Hill, NY.

Popescu, M., 2009. Modeling of fluid dynamics interacting with ductile fraction propagation in high pressure pipeline. Acta Mech. Sin. 25 (3), 311–318.

Rendleman, C.A., Beckner, V.E., Lijewski, M., Crutchfield, W., Bell, J.B., 2000. Parallelization of structured, hierarchical adaptive mesh refinement algorithms. Comput. Visual. Sci. 3 (3), 147–157.

Roussanaly, S., Bureau-Cauchois, G., Husebye, J., 2013. Costs benchmark of CO_2 transport technologies for a group of various size industries. Int. J. Greenh. Gas Control 12, 341–350.

Span, R., Wagner, W., 1996. A new equation of state for carbon dioxide covering the fluid region from the triple-point temperature to 1100 K at pressures up to 800 MPa. J. Phys. Chem. Ref. Data 25 (6).

Stewart, H.B., Wendroff, B., 1984. Two-phase flow: models and methods. J. Comput. Phys. 56 (3), 363–409 (http://www.sciencedirect.com/science/article/pii/0021999184901037).

Stuhmiller, J., 1977. The influence of interfacial pressure forces on the character of two-phase flow model equations. Int. J. Multiphase Flow 3 (6), 551–560.

Terenzi, A., 2005. Influence of real-fluid properties in modeling decompression wave interacting with ductile fracture propagation. Oil Gas Sci. Technol. 60 (4), 711–719.

Thome, J., Ribatski, G., 2005. State-of-the-Art Review of Flow Boiling and Two-Phase Flow of CO_2 in macro- and micro- channels. Int. J. Refrig. 28 (8), 1149–1168.

Yeom, G.-S., Chang, K.-S., 2013. A modified HLLC-type Riemann solver for the compressible six-equation two-fluid model. Comput Fluids 76, 86–104.

Ziegler, U., 2008. The NIRVANA code: parallel computational MHD with adaptive mesh refinement. Comput. Phys. Commun. 179, 224–227.